RF Information Harvesting for Medium Access in Event-driven Batteryless Sensing

N. H. Hokke[*], S. Sharma[∇], R.V. Prasad[∇], L. Mottola[#], S. Narayana[∇], V. Rao[§], N. Kouvelas[∇]
[*]Zero Energy Development B.V., [∇]Delft University of Technology, [#]Politecnico di Milano, [§]Cognizant

ABSTRACT

We present *radio-frequency (RF) information harvesting*, a channel sensing technique that takes advantage of the energy in the wireless medium to detect channel activity at essentially no energy cost. RF information harvesting is essential for event-driven wireless sensing applications using battery-less devices that harvest tiny amounts of energy from impromptu events, such as operating a switch, and then transmit the event notification to a one-hop gateway. As multiple such devices may concurrently detect events, coordinating access to the channel is key. RF information harvesting allows devices to break the symmetry between concurrently-transmitting devices based on the harvested energy from the ongoing transmissions. To demonstrate the benefits of RF information harvesting, we integrate it in a tailor-made ultra low-power hardware MAC protocol we call *Radio Frequency-Distance Packet Queuing (RF-DiPaQ)*. We build a hardware/software prototype of RF-DiPaQ and use an established Markov framework to study its performance at scale. Comparing RF-DiPaQ against staple contention-based MAC protocols, we show that it outperforms pure Aloha and 1-CSMA by factors of 3.55 and 1.21 respectively in throughput, while it saturates at more than double the offered load compared to 1-CSMA. As traffic increases, the energy saving of RF-DiPaQ against CSMA protocols increases, consuming 36% less energy than np-CSMA at typical offered loads.

1 INTRODUCTION

Industry interest in wireless sensing is rising. For example, Airbus[1] is leading the efforts towards smart cabins, where wireless sensing is expected not only to contribute to better flying experiences but also to help airliners reduce costs. The losses for airliners due to mid-air injuries from falling baggage and severe turbulences as seat belts are not properly fastened and lost equipment are in the order of hundreds of millions of dollars, including lost workdays of crew[2]. Particularly, the crew is at risk during turbulences as they need to manually inspect if passengers have fastened their seat belts. Wireless sensing is expected to improve safety by checking whether seat belts are fastened and overhead bins are latched.

Fig. 1 shows examples of this emerging class of wireless sensing event-driven applications. A large number of embedded devices are closely co-located and must rapidly report notifications regarding events of interest, for example, toggling a mechanical switch that signals a fastened seat belt. These events are likely to occur almost simultaneously.

[1]https://www.airbus.com/en/newsroom/stories/2019-07-iot-aerospaces-great-new-connector (accessed: 2021-09-08)
[2]https://www.telegraph.co.uk/travel/travel-truths/products-you-can-take-from-an-airline/ (accessed: 2021-10-02)

[*]N.H.Hokke@ZED-IoT.com.

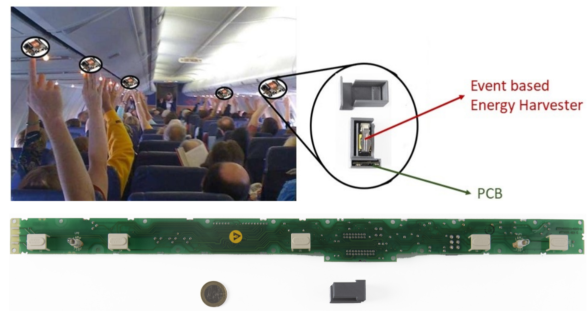

Fig. 1. Example of event-driven energy harvesting wireless sensing application: passengers flight attendant call buttons. The top figure shows our switch with 3D printed package. The bottom figure shows an actual PCB used for calling buttons in flights. The idea is to replace these with our miniature wireless event-driven energy-harvesting switches.

The notifications are to be reported wirelessly to a 1-hop gateway. However, the sensing devices cannot be powered through batteries due to safety regulations. If powered through cable harnesses, the increased fuel and maintenance costs would outweigh the advantages brought by wireless sensing [1]. The only alternative is to provision energy through ambient harvesting; yet, limited form factors pose extreme constraints on system design. The amount of energy harvested is minimal, for example, ≈200 μJ from the operation of a mechanical switch, while the time for the harvested energy to completely dissipate is in the order of ms. Moreover, unlike traditional embedded sensing, devices remain off until the next harvesting event.

Albeit our original motivation is rooted in aircraft industry, this technology is applicable to other domains sharing similar features, including logistics and industrial IoT. In these scenarios, vibrations may be used to power wireless sensors attached to packages that monitor physical quantities during travel [2] or embed sensor in the body of equipment in industries to measure vital operational parameters [3, 4].

Challenges. The tiny energy budgets in energy harvesting system –sufficient only for a couple of transmissions at best– with unpredictable data generation times pose substantial challenges for handling channel contention. Central coordination in these settings is plainly infeasible and calls for a novel distributed energy-aware approach. The strategy employed to this end must adhere to these energy constraints and yet function in an event-driven mode. The stringent energy budgets make Aloha-like medium access protocols a natural choice. However, Aloha has low channel efficiency.

The simultaneity of events compounds the problem, as it leads to contention on the wireless channel and may eventually result in

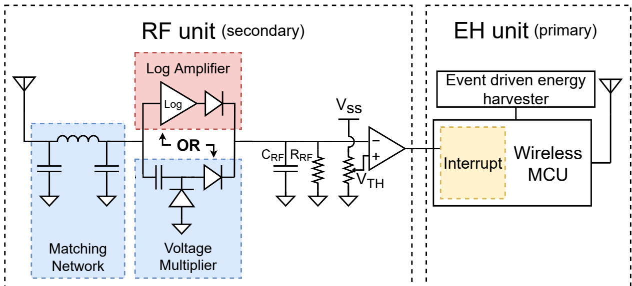

Fig. 2. Hardware schematic of an RF-DiPaQ sensor showing both the RF unit and the EH unit

packet collisions and data loss. Opting for a Carrier-Sense Multiple-Access (CSMA) mechanisms is next to impossible because of the limited energy, devices can hardly afford the luxury of actively sensing the channel and harvested energy is likely to be insufficient to keep the node operational for long. Despite existing works on adaptive duty cycling for energy-harvesting sensors [5, 6] and specific MAC protocols for energy-harvesting wireless networks [7], energy-harvesting systems that are completely event-driven lack the fundamental mechanisms to handle channel contention.

RF information harvesting. Working with the challenges posed by the nature of such systems, we devise a notion of *radio-frequency (RF) information harvesting* to address these issues. Through special-purpose hardware support, the idea is to infer information on channel occupancy by harvesting energy from ongoing transmissions and break the symmetry between concurrently-transmitting devices. This provides a way to avoid collisions by deferring the upcoming transmissions at different devices.

To demonstrate the benefits of RF information harvesting, we integrate it in an ultra low-power MAC protocol expressly conceived for batteryless energy-harvesting event-driven wireless sensing that we call Radio Frequency-Distance Packet Queuing (RF-DiPaQ). Fig. 2 presents the hardware overview of a RF-DiPaQ sensor, where two coordinated units are integrated:

(1) *energy-harvesting (EH) unit*: it is the primary harvester, which scavenges energy from an event, stores it temporarily, and uses it only to transmit the event notification. The harvested energy is thus barely sufficient to transmit a single packet, without any energy left for other functionality.
(2) *radio-frequency (RF) unit:* it is the secondary harvester, which involves an RF-harvesting antenna, a matching circuit, and a reference capacitor circuit that effectively represents a hardware implementation of RF information harvesting. The harvesting antenna scavenges energy whenever it receives a carrier-wave from another device in the vicinity transmitting a packet. Using a Wake-up Radio (WuR)-like receiver circuit, the reference capacitor C_{RF} is charged, which is otherwise discharged by resistor R_{RF}. When the reference capacitor C_{RF} discharges below a threshold, an idle channel is assessed, possibly triggering a packet transmission.

The incoming RF is amplified using either a voltage multiplier circuit comprising of passive components or a log amplifier (active device) as shown in Fig. 2. The log amplifier and voltage multiplier are mutually exclusive.

The main focus of this article is to exploit RF information harvesting and work around the extremely tight energy constraints in order to design an effective medium access mechanism. The key to the efficient performance that RF information harvesting enables is in the functioning of the RF unit in situations of high channel contention. Because of the different packet transmission times, the spatial dispersion of transmitters, and varied path losses, the reference capacitors at C_{RF} at different RF-DiPaQ devices accumulate different amounts of energy. When discharging over resistor R_{RF}, the threshold, triggering packet transmissions is crossed at different points in time at different devices. The first node that transmits causes the charges in the C_{RF}'s to rise again, resulting in all nodes that did not transmit to compete for channel access at a later time. This introduces a form of temporal diversity that de-synchronizes packet transmissions, effectively resolving collisions.

Notably, *no additional energy* than the one used for packet transmissions is spent anywhere in this operation. The processing repeats until the last RF-DiPaQ device transmits the pending packet. In a way, this mechanism is similar to the use of variable-sized colliding packet probes in receiver-initiated MAC protocols [8], but operates without the need of dedicated packet transmissions and thus incurs essentially no energy overhead.

Based on the operation of the RF unit, RF-DiPaQ devices refrain from transmitting until the medium is sensed idle, then transmit unconditionally, namely, they function akin to a 1-CSMA schema. However, contrary to 1-CSMA, which requires the medium to be continuously sensed by the device pending to transmit, RF-DiPaQ simply observes the reference capacitor voltage, which is charged by devices currently occupying the medium.

As a result of our design, networks using RF-DiPaQ enjoy the increased throughput offered by CSMA protocols, without the energy overhead of continuous channel sensing. Furthermore, contrary to CSMA protocols where channel sensing only occurs in the presence of pending transmissions, RF information harvesting is performed continuously: the reference capacitor constantly represents the current state of the channel, even before the main energy harvesting event occurs. This enables a node to gain a better snapshot of the channel conditions at the time an event occurs.

Contribution. Our *fundamental contributions* are to introduce the concept of RF information harvesting to monitor channel occupancy without using the primary harvester and to design and implement an ultra low-power MAC protocol for networks of event-driven energy-harvesting wireless sensing devices. A secondary novelty of this work is using the property of differential energy envelopes as a contention resolution mechanism over the existing RF harvesting/wakeup radio circuits. To the best of our knowledge, we are the first to use the amount of harvested RF energy for MAC operation. The core of our technical work is reported in Sec. 3.

Our evaluation of the performance of RF information harvesting builds upon three pillars:

(1) an analytical model of the behavior of RF information harvesting in a low-power wireless protocol that allows us to determine performance at scale by deriving the probabilities of successful transmissions, throughput, and success rate, as illustrated in Sec. 4;

(2) a real-world hardware prototype, illustrated in Sec. 5, which doubles as an instrument to validate both the model of Sec. 4 and as a foundation for real-world experiments;
(3) a hybrid simulation environment, described in Sec. 6, created by combining a network simulator and an analog one, both required to obtain accurate results as the operation of RF-DiPaQ extends across hardware and software.

Using the analytical model, the hybrid simulator, and the hardware prototype, we conduct an extensive evaluation of the performance of RF information harvesting when integrated in RF-DiPaQ. We report our findings in Sec. 7, for example, RF-DiPaQ outperforms pure Aloha and 1-CSMA by factors of 3.55 and 1.21 respectively in terms of throughput, while it saturates at more than double the offered load compared to 1-CSMA. As traffic increases, the energy savings achieved by RF-DiPaQ against CSMA protocols increase, consuming 36% less energy than np-CSMA at high offered load, showcasing its ability to scale.

2 RELATED WORK

There has been substantial work done in the field of RF harvesting and multiple solutions exist which leverage RF energy to partly cover the system's energy needs [9], using the same RF front-end for both energy harvesting and communication. The focus is on finding the optimal time division between harvesting and transmission to maximize throughput and energy efficiency [3, 10–14]. In contrast, we use RF harvesting not as a supplementary source of energy for the system but instead as a channel sensing mechanism. The related hardware developed is exclusively used to this end and we leave the choice of harvesting technology used as the primary unit to be orthogonal to our mechanism. Further, even though RF-DiPaQ is instrumental for us to show the applicability of RF information harvesting for channel sensing, the applicability of the latter extends beyond RF-DiPaQ. For example, receiver-initiated MAC protocols [8] often employ CCA-based rendezvous to reduce idle listening. RF information harvesting may be used as a replacement for that, reducing energy consumption and delay.

Our hardware implementation of RF information harvesting shares similarities with Wake-up Radios (WuR). Many WuR receivers exist using minimum active components with up to -56 dBm sensitivity while consuming around 1 μW in ISM bands [15–21]. WuR-based devices trigger the operation of the main computing and communication unit when a wake-up command is received on the WuR front-end [22]. The role of RF information harvesting is essentially different. Instead of requiring an explicit command to trigger the operation of another unit, RF information harvesting efficiently provides continuous information on channel occupancy based on current ongoing transmissions.

These fundamental building-blocks are often integrated into full-fledged MAC protocols to demonstrate the overall benefits, as we do when integrating RF information harvesting in RF-DiPaQ. For example, many MAC protocols are especially optimized for RF harvesting [3, 10–14] or use WuRs to reduce the energy cost of idle-listening [17–19, 23, 24]. Fig. 3 presents a qualitative comparison. Unlike our work, because of the single front-end used for energy harvesting and communication, protocols using RF harvesting struggle to adapt to changes in network topology, number of devices, and/or periodicity of transmissions. Further, not even when using WuR devices [17–19, 23], the energy consumed per transmission reaches the performance we achieve by using RF information harvesting in RF-DiPaQ.

	Throughput per Node	Normalized Throughput	Energy per Transmission	Overhead, feedback	Gateway Dependence	Semantic Addressing	Evaluation Type
Kwan [3]	6.4 bps	-	0.4-0.6 mJ	+2 B/pkt	High	Yes	**E, S**
Naderi [11]	320 bps	-	CS	RTS/CTS, ACK	Medium	No	**E, S**
Hoang [12]	-	0.45	CS	RTS/CTS, ACK, beacons	High	No	**N**
Bae [13]	-	0.16	CS	RTS/CTS, ACK	Medium	No	**N**
Ha [14]	40 bps	-	CS	RTS/CTS, ACK, beacons	High	Yes	**S**
Le [18]	64-68 bps	-	1.3-1.6 mJ	WuR-beacons, ACK	Medium	Yes	**S**
Karvonen [23]	64-68 bps	-	$\simeq$ 3.17 mJ	WuR-beacons, ACK	Medium	Yes	**S**
Oller [19]	144 bps	-	$\simeq$ 5.27 mJ	WuR-beacons, ACK	Medium	Yes	**S**
RF-DiPaQ	286 bps	0.64	0.4-0.6 mJ	zero	No	No	**E, S, N**

Fig. 3. Qualitative comparison of RF-DiPaQ with MAC protocols using RF harvesting or WuR receivers, the values of (normalized) throughput per node are at saturation. (E is Experimental, S is Simulated, N is Numerical).

Note that our system may be, in a sense, considered as an intermittent computing system [25]. However, the application processing in our case only includes a single atomic operation for transmitting the event data, and no application state is to be carried over to the next device activation. Therefore, the variety of techniques that use the persistent state to cross periods of energy unavailability are unnecessary here [26].In a sense, RF information harvesting is also akin to backscatter communications [27]. RF information harvesting, however, is not in charge of communicating application data, regardless of the specific technique employed to that end, but merely acts as a channel sensing mechanism. Also, backscatter communications may not instantly catch the event and requires a more number of high-power transmitters to poll events, unlike RF-DiPaQ.

3 RF INFORMATION HARVESTING

The operation of our hardware implementation of RF information harvesting is deceptively simple. The received carrier wave is rectified by a RF harvesting circuit and used to charge a reference capacitor C_{RF}, which is continuously being discharged by a corresponding resistor R_{RF}, as shown in Fig. 2. This results in the voltage across C_{RF}, denoted by V_{RF}, to vary depending on channel activity. We compare V_{RF} to a close-to-zero voltage-threshold V_{TH}. When a carrier wave is being received, V_{RF} exceeds V_{TH}, indicating that a transmitter is utilizing the channel. With no carrier wave, V_{RF} drops below V_{TH}, indicating a clear channel.

The impact of this operation when integrated in a complete MAC protocol and at scale, however, is less straightforward. As we use RF information harvesting for channel sensing in RF-DiPaQ, the latter offers a way to investigate this aspect. In essence, RF-DiPaQ is a simple carrier-sense multiple access MAC protocol that uses RF information harvesting for channel sensing, and is especially optimized for that. It is the conceptual and practical instrument we use to investigate the impact of RF information harvesting on the whole system performance.

Fig. 4 illustrates an example execution, showing RF activity and the temporal variation of V_{RF} at three nodes, denoted as N1, N2, and N3. MAC frames arriving locally from higher layers in the stack are indicated by upward-pointing arrows and the *TX* block indicates

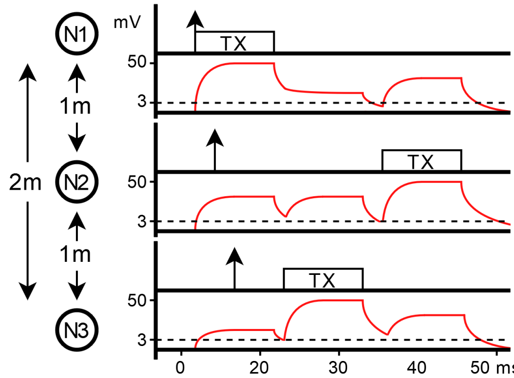

Fig. 4. RF activity and charge in C_{RF} over time for three transmitting nodes, under the RF-DiPaQ protocol.

packet transmissions. For simplicity of illustration, say the nodes are placed linearly 1 m apart and V_{TH} = 3 mV. The first packet to arrive at N1 is transmitted immediately: V_{RF} is below the V_{TH} = 3 mV and so the channel is considered clear. As the transmission progresses, V_{RF} at the other two nodes grows according to the distance from N1; smaller distances imply higher voltage and vice-versa. Meanwhile, MAC frames arrive at N2, N3 from the higher layers in the stack. Once N1's transmission is complete, V_{RF} at all nodes drops as the capacitor C_{RF} discharges over resistor R_{RF}.

Due to the lower initial value, V_{RF} of N3 drops below V_{TH} first. As a node with pending traffic checks the state of the channel before transmitting, N3 finds the channel clear before N2 and commences the transmission. This causes V_{RF} across the other two nodes to rise again, further postponing N2's transmission. Once N3 completes its transmission, V_{RF} at N2 eventually drops below V_{TH} too, causing N2's transmission to begin. In principle, two or more nodes that experience the exact same propagation effects from a transmitter may reach the same V_{RF}, causing their transmissions to commence simultaneously, yielding a collision. In practice, due to multi-path fading and the presence of (moving) obstacles, these situations are extremely unlikely.

Note that channel sensing through RF information harvesting may occur independently of the MCU operation, even when the latter is not powered. The orthogonality of the two is reflected in the hardware design for RF-DiPaQ devices, depicted in Fig. 2. The EH unit is only dedicated to sensing and utilizes the RF unit strictly for channel sensing, while the two units remain decoupled also in energy provisioning. The antenna used for RF information harvesting may also be used to power the EH unit to reduce footprint, but due to the need for an RF switch, this would also decrease the receive sensitivity.

4 ANALYTICAL MODEL

First, we study the benefits of RF information harvesting by adopting Markov framework to the network of RF-DiPaQ devices, since it is a well-known tool used to model complex systems. We, then model our RF information harvesting by using the exponential discharge curves of capacitors which is a key element in determining the network behavior. This model is instrumental to evaluate throughput and packet success rate for a given offered load g [28] and in finding the theoretical limits that are difficult to find with

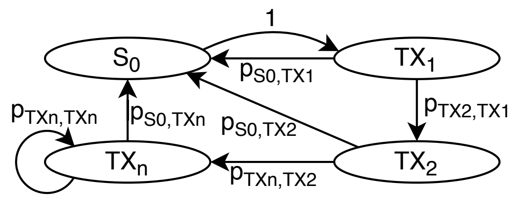

Fig. 5. Markov model of a network of RF-DiPaQ devices.

From	To	Condition
S_0	TX_1	$\sum_P = 1 \wedge \forall c \in C : c < V_{TH}$
TX_1	S_0	$\sum_P = 0 \wedge \forall c \in C : c < V_{TH}$
TX_1	TX_2	$\sum_P > 0 \wedge min(C_p) = V_{TH}$
TX_2	S_0	$\sum_P = 0 \wedge \forall c \in C : c < V_{TH}$
TX_2	TX_n	$\sum_P > 0 \wedge min(C_p) = V_{TH}$
TX_n	S_0	$\sum_P = 0 \wedge \forall c \in C : c < V_{TH}$
TX_n	TX_n	$\sum_P > 0 \wedge min(C_p) = V_{TH}$

Fig. 6. Conditions for state transitions.

real-life measurements. This Markov model helps further in designing the network.

4.1 Model Overview

The model represents the behavior of the whole network and includes four states, shown in Fig. 5. In the S_0 state, there are no packets/events in the system and all charges in the reference capacitors C_{RF} are below V_{TH}. The S_0 state is always followed by TX_1, the first transmission state, as a result of the first packet generation and corresponding transmission. Following the first transmission, in state TX_2 or TX_n the devices compare the charge in the reference capacitors C_{RF} against the threshold V_{TH}.

Fig. 6 summarizes the conditions for state transition, with $\sum_P$ being the total number of pending packets, C the set of charge levels in all reference capacitors C_{RF}, and $C_p \in C$ is the set of charges in the reference capacitors C_{RF} at nodes with pending packets. In the presence of pending packets, the moment the lowest charged capacitor hits V_{TH} and commits to transmit, the network transitions to the following transmission state. All states transition back to S_0 when there are no more pending packets and all capacitors are charged below V_{TH}. Fig. 7 shows an example execution illustrating how the time of packet arrivals, the time a node commits to transmit, and how discharge times align with the state transitions.

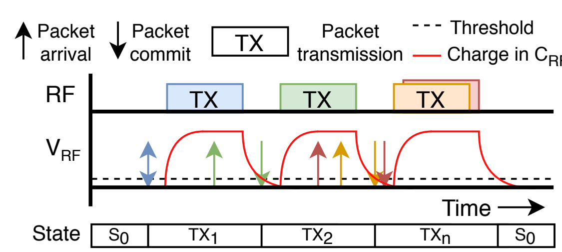

Fig. 7. Illustration of states transitions over time while packets arrive and its effect on V_{RF}.

To quantify the network performance, we can calculate the system throughput T_h and packet success rate S as

$$T_h = \frac{\sum_{i=0}^{3} \pi^i \cdot T \cdot P(\text{success at } i)}{\sum_{i=0}^{3} \pi^i \cdot \underline{T^i}}, \tag{1a}$$

$$S = T_h / g, \tag{1b}$$

where g is offered load, π^i are the steady-state probabilities, T is packet transmission time, and $P(\text{success at } i)$ are the success probabilities at state i, with i being S_0, TX_1, TX_2, or TX_n.

In the following, we derive analytical expressions for steady-state probabilities π^i and the state success probabilities. In turn, these require quantifying the time for capacitor discharge and the duration of individual states.

4.2 Capacitor Discharge Time

Let us call T_{rc} the interval of time between the end of a transmission and the moment the charge in C_{RF} reaches V_{TH}.

This time depends on the amount of charge in C_{RF} accumulated during previous transmission, on the RC value determined by C_{RF} and R_{RF} values, and on the value of V_{TH}. We express the charge in C_{RF} as the voltage level V due to input power P_{in} [16], $V = 10^{a \cdot P_{in} + b}$ with a, b being hardware constants.

Using the path-loss model, we express P_{in} as a function of distance d from the transmitter, resulting in

$$\begin{aligned} V = l d^k, \quad \text{where } k = -a10\gamma, l = 10^e, \\ e = a(P_{tx} - P_{l0} + 10\gamma log_{10}(d_0)) + b, \end{aligned} \tag{2}$$

where the values of k and l may be empirically determined, γ is path loss exponent, P_{tx} is transmitted power, P_{l0} is path loss in decibels (dB) at the reference distance d_0.

As the discharge of C_{RF} follows an exponential RC curve, we express T_{rc} in terms of the value of a random variable D representing the distance from the transmitter

$$T_{rc} = \frac{RC}{T} \cdot ln\left(\frac{D^k \cdot l}{V_{TH}}\right) \tag{3}$$

Thus, T_{rc} may be seen as a transformation of a random variable D according to a certain function $h(d)$. If the distribution of D is known, we compute the probability density function (PDF) and cumulative distribution function (CDF) of T_{rc} as

$$f_{T_{rc}}(t) = -f_D(h^{-1}(t)) \frac{\delta}{\delta t} h^{-1}(t), \tag{4}$$

$$F_{T_{rc}}(t) = 1 - F_D(h^{-1}(t)), \tag{5}$$

where indeed function h is the transformation of D into T_{rc}.

4.3 State Duration

The time spent in a transmission state is the sum of four time segments, as shown in Fig. 8, which together contribute to the expected time $\underline{T^i}$ spent in state i, thus

$$\underline{T^i} = \underline{y^i} + \tau + T + \underline{T^i_{rc}}, \tag{6}$$

where the individual quantities are determined as follows. As the radio takes time to stabilize before transmitting, there exists a *vulnerable time* between when a node finds the channel clear and when the transmission actually commences. Say the time for the radio to stabilize is r; we call $\tau = \frac{r}{T}$ the time for the radio to stabilize normalized to the packet transmission time T. Note that τ and T are constants determined by the chosen radio and packet structure. Because the reference capacitors are only charged when a transmission actually occurs, any other arrival within τ results in a collision. Therefore, y represents the difference in time between the first and last arrival within the vulnerable period τ. Finally, T_{rc} represents the discharge time at the lowest-charged node with pending packets; if no node has pending packets, it however represents the longest discharge time across the whole system.

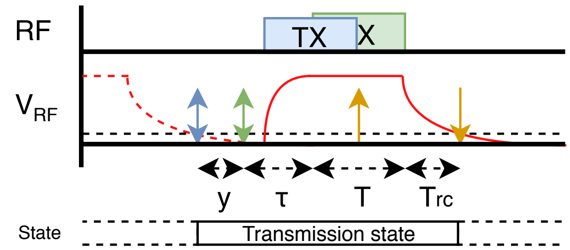

Fig. 8. Close-up view of a slice of Fig. 7 showing the individual time segments contributing to the duration of a state transmission.

In state TX_1, the CDF of y^{TX_1} equals the probability of no packet arrivals in the time interval $\tau - t$. The CDF can be differentiated to find the PDF, which determines the expected value of y^{TX_1} as $\underline{y^{TX_1}} = \tau - (1 - e^{-g\tau})/g$. In state $TX_{\geq 2}$, y^{TX_2} and y^{TX_n} depend on the sum of the number of packets still pending and of the new packet arrivals within the τ interval experienced in the current state. The probability of the last discharge time to fall within time τ equals the PDF of $y^{TX_{2,n}}$, and as above it may be used to find the expected value of $y^{TX_{2,n}}$ as,

$$\underline{y^{TX_{\geq 2}}} = \sum_{n=2}^{N} P(N_{TX_{\geq 2}} = n) \int_{0+}^{\tau} t \cdot P(y^{TX_{\geq 2}} = t | n) dt, \tag{7}$$

$$P(N_{TX_{\geq 2}} = n) = \frac{\sum_{q=1}^{n} P(q \text{ in } \underline{T_{-1}} - \tau) \cdot P((n-q) \text{ in } \tau)}{\sum_{r=1}^{N} \sum_{q=1}^{r} P(q \text{ in } \underline{T_{-1}} - \tau) \cdot P((r-q) \text{ in } \tau)}, \tag{8}$$

which shows how to calculate the probability of having n pending nodes at time τ into the $TX_{\geq 2}$ states, where $P(x \text{ in } t)$ describes the probability of x arrivals in time t ,which can be modeled using the Poisson PDF, and $\underline{T_{-1}}$ denotes the time duration of the previous state that equals $\underline{T^{TX_1}}$ and $\underline{T^{TX_2}}$ for TX_2 and TX_n, respectively.

When transitioning back to the S_0 state, $T_{rc} = T_{rc,0}$ takes is the longest discharge time across the whole system, as in this situation no nodes have pending packets waiting to be transmitted. The expected value of the maximum of multiple samples of the same distribution is found using order statistics [29] as $\underline{T_{rc,0}} = \int_0^\infty x N f_{T_{rc}}(x) \cdot F_{T_{rc}}(x)^{N-1} dx$, else, when at least one node has pending packets, $T_{rc} = T_{rc,1}$ is the discharge time of the lowest-charged node, which is calculated as $\underline{T_{rc,1} | n} = \int_0^\infty x \cdot n \cdot f_{T_{rc}}(x) \cdot (1 - F_{T_{rc}}(x))^{n-1} dx$. To compute $\underline{T_{rc,1}}$, we need to determine the probability of the state ending with n nodes with pending packets. The packet arrivals during the first τ time of state TX_1 result in immediate transmissions, so this probability equals the probability of n arrivals in the remaining $\underline{T^{TX_1}} - \tau$ time. As $\underline{T_{rc}}$ is part of this time and is yet unknown, an estimate is needed. For state TX_1, $\underline{T_{rc,0}}$ is used in the estimation of $\underline{T^{TX_1}} - \tau$ as given in Eq. 9. When the offered load g is small, the network is mostly in the TX_1 state, and the probability of transitioning to the S_0 state is higher than moving to TX_2, resulting in $\underline{T_{rc,0}}$. For state $TX_{\geq 2}$, we use $\underline{T_{rc,1}|n=1}$ as an estimation to find $\underline{T^{TX_{\geq 2}}} - \tau$; $n = 1$ represents the smallest number of pending nodes resulting in the largest possible $\underline{T_{rc,1}}$.

$$\underline{T^{TX_1}} - \tau \approx \underline{T^{TX_1}_{\text{est}}} = \underline{y^{TX_1}} + T + \underline{T_{rc,0}} \tag{9}$$

$$\underline{T^{TX_{2,n}}} - \tau \approx \underline{T^{TX_{2,n}}_{\text{est}}} = \underline{y^{TX_{2,n}}} + T + \underline{T^{TX_{2,n}}_{rc,1}|n=1} \tag{10}$$

Based on the estimates, the probability of the state ending with n pending nodes can be calculated. Given that the states end with one or more pending nodes, there must have been at least one, and at most N arrivals. So the probability of n arrivals must be divided by the sum of probabilities of one to N arrivals. This is calculated using the function $A(n, t, m)$ given by Eq. 11, which calculates the probability of n arrivals in time t, for at least m and at most N arrivals. Knowing the probabilities of ending with n arrivals for each state, each $\underline{T_{rc,1}}$ is calculated based on the estimates as below,

$$P(N_{\underline{T^i_{\text{est}}}} = n) = A(n, \underline{T^i_{\text{est}}}, 1), \tag{11}$$

$$A(n, t, m) = \frac{P(n \text{ in } t)}{\sum_{i=m}^{N} P(i \text{ in } t)}, \tag{12}$$

$$\underline{T^i_{rc,1}} = \sum_{n=1}^{N} A(n, \underline{T^i_{\text{est}}}, 1) \cdot \underline{T^i_{rc,1}|n}. \tag{13}$$

With the expected value of $T^i_{rc,0}$ and $T^i_{rc,1}$ for all transmission states known, the $\underline{T_{rc}}$ can be calculated using Eq. 14. Where P^i_0 and P^i_1 are,

$$\underline{T^i_{rc}} = P_0 \cdot \underline{T_{rc,0}} + P_1 \cdot \underline{T^i_{rc,1}} \tag{14}$$

$$P^i_1 = 1 - P^i_0 = 1 - A(0, \underline{T^i_{\text{est}}}, 0). \tag{15}$$

With $\underline{y}$ and $\underline{T_{rc}}$ for all transmission states known, the average time spent in each state can be calculated using Eq. 6.

4.4 State Success Probability

As, in state TX_1, the voltage in the reference capacitors only starts rising τ time after the first arrival starting the state, once the first packet is transmitted, any other arrival within this time period will collide with the first packet. This results in the probability of success of the TX_1 state, $P(\text{s at } TX_1)$, equaling the probability of no arrivals within τ, which is calculated with function $A(n, t, m)$ (Eq. 12) as, $P(\text{s at } TX_1) = A(0, \tau, 0)$. The probability of success in the $TX_{2,n}$ states is based on the effect described in Sec. 3. The state is successful when the difference in discharge times of the two lowest charged nodes with a pending packet is larger than time τ (discharge time is modeled by T_{rc} as seen in Eq. 4 and Eq. 5). The probability of success knowing that n nodes are waiting to transmit at time τ in state, $P(\text{s at } TX_{2,n}|n)$ is given in Eq. 16. Taking into account the probability of n pending nodes at time τ (Eq. 8) the probability of success for both $TX_{2,n}$ states, is represented by $P(\text{s at } TX_{2,n})$, and can be calculated as,

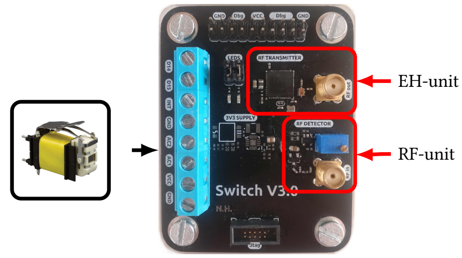

Fig. 9. Switch V3.0, our prototype wireless sensor running RF-DiPaQ with RF information harvesting.

$$P(\text{s at } TX_{2,n}|n) = \int_0^\infty n \cdot f_{T_{rc}}(x) \cdot (1 - F_{T_{rc}}(x+\tau))^{n-1} dx \quad (\text{for } n \geq 1), \tag{16}$$

$$P(\text{s at } TX_{2,n}) = \sum_{n=1}^{N} P(N_{TX_{\geq 2}} = n) \cdot P(\text{s at } TX_{2,n}|n). \tag{17}$$

4.5 Steady State Probability

To calculate the model throughput and success rate, the steady state probabilities can be computed by solving the linear equations resulting from all state transition probabilities (Fig. 5). The system can then be solved in terms of p_{TX_2,TX_1}, p_{TX_n,TX_2}, and p_{TX_n,TX_n}, which can be calculated using function $A(n, t, m)$ found in Eq. 12 as given in the following equations,

$$\begin{aligned} p_{TX_2,TX_1} &= 1 - P(\text{no arrivals in } \underline{T^{TX_1}} - \tau) \\ &= 1 - A(0, \underline{T^{TX_1}} - \tau, 0) \end{aligned} \tag{18a}$$

$$p_{TX_n,TX_2} = 1 - A(0, \underline{T^{TX_2}} - \tau, 0) \tag{18b}$$

$$p_{TX_n,TX_n} = 1 - A(0, \underline{T^{TX_n}} - \tau, 0) \tag{18c}$$

This now allows us to use Eq. 1a and Eq. 1b to model the throughput and success rate of RF-DiPaQ, at offered load g.

5 PROTOTYPE

We build a hardware and software prototype to study the real-world behavior of RF information harvesting in RF-DiPaQ, shown in Fig. 9. We describe the system design next, along with the validation efforts that our prototype enables.

Hardware design. Our Switch V3.0 can capture events when connected to mechanical harvesters, such as vibration and switches. Fig. 9 shows AFIG-0007 from ZF switches, a push-button type energy harvester module (ref. design from TI [30]). The energy generated by a single press and release of the button was measured on an average to be 420μJ. With this energy, our Switch V3.0 is functional up to one second.

To realize the RF unit, as shown in Fig. 2, we base our design on that of Nintanavongsa *et al.* [31]. The antenna is connected to a pi-matching network that tunes the RF unit to the specific carrier wave frequency. Using a mutually exclusive single-stage voltage multiplier or a log amplifier, the RF signal is rectified, boosted, and used to charge capacitor C_{RF}. The choice of selecting voltage multiplier or log amplifier is up to the designer depending on the use case. While voltage multiplier is completely passive, log amplifier

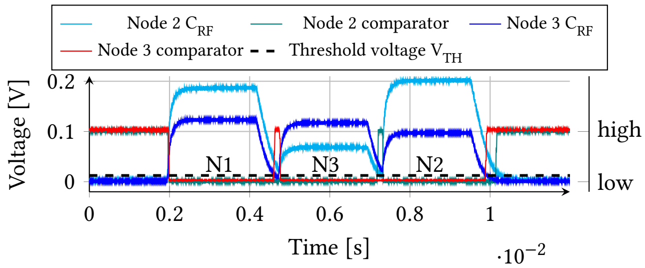

Fig. 10. The scenario of Fig. 4 with Switch V3.0 prototypes. The plot reports the measured voltage in the capacitors C_{RF} of N2 and N3 in Fig. 4, along with their digital comparator outputs (scaled down) over time.

requires power from the EH unit to function. However, log amplifier assists in sensing channel over longer ranges -up to 15 m when compared with voltage multiplier -up to 1.5 m. Hence, voltage multiplier can be used when the amount of harvested energy is relatively low and the nodes are nearby; log amplifier enables longer range at the cost of operating power.

Resistor R_{RF} discharges C_{RF} when no carrier wave is received. An inverting comparator compares the voltage in C_{RF} to the threshold voltage V_{TH}, which may be tuned through a potentiometer. The comparator outputs a digital high signal whenever the voltage in C_{RF} is lower than V_{TH} and a digital low signal otherwise. The digital output of the comparator is connected to an interrupt pin of the microcontroller unit (MCU).

We use TI's CC1352R [32] as MCU. We program the device to transmit event information immediately, if the comparator output is high, or to sleep until a rising flank, and then transmit.

Sample execution. We replicate the scenario in Fig. 4 using three nodes N1, N2, and N3. N1 initially transmits a packet, whereas N2 and N3 trigger a new packet transmission while N1 is transmitting. As the three transmissions overlap in time within the same broadcast domain, this setting would normally cause collisions.

In contrast, Fig. 10 illustrates the operation of Switch V3.0 in this scenario. The plot shows the voltage measured over time across the capacitor of N2 (light blue) and N3 (dark blue), along with the digital output of the voltage comparators of N2 (teal) and of N3 (red). We indicate with C^{n}_{RF} the charge of the C_{RF} capacitor at node n. The initial transmission of N1, indicated with "N1", makes the voltage levels at both C^{2}_{RF} and C^{3}_{RF} rise. As N2 is physically closer to N1 compared to N3, C^{2}_{RF} accumulates a higher charge. When N1 completes the transmission, the charge in both capacitors starts dropping, yet C^{3}_{RF} reaches the threshold voltage V_{TH} first.

The moment the voltage of C^{3}_{RF} is at V_{TH}, the comparator at N3 outputs a digital high signal, granting N3 permission to transmit. This transmission, indicated with "N3" in the plot, causes the voltages in the capacitors to rise again, critically before C^{2}_{RF} reaches V_{TH}, consequently causing the comparator at N2 to keep emitting a digital low signal. As soon as N3 completes the transmission, the voltage in C^{2}_{RF} eventually reaches V_{TH} while discharging, causing the N2 comparator to output a digital high signal. As seen earlier for N3, this grants N2 permission to transmit. The transmission of N2, indicated with "N2" in the plot, again causes all capacitors C_{RF} to charge. As there are no more packets to transmit, once N2 completes the transmission, the voltage levels of all capacitors C_{RF} eventually drop to zero, causing all comparators to output a digital high signal, indicating an idle channel.

Parameter	Value	Parameter	Value
V_{TH}	0.003 V	RC	0.0050 s
k	-1.146	T	0.01792 s
l	0.0334	τ	0.0084

Fig. 11. Model parameters, including those empirically determined using the SwitchV3.0 prototype.

Fig. 12. A network of 30 SwitchV3.0 nodes and gateway in a 4 m by 4 m area emulating multiple harvester events per second.

Model validation. To instantiate the model of Sec. 4, we empirically determine the values of k and l in Eq. 2 by placing nine uniformly-spaced SwitchV3.0 on a line. We instruct them to transmit sequentially to the first node in the line, which measures the voltage across its capacitor C_{RF} for each received packet. This allows us to collect sparse knowledge on the relation between the voltage across C_{RF} and distance. We fit Eq. 2 to this data to find the value of k and l. In our prototype, the threshold voltage V_{TH} is set to 3 mV and the RC value to 0.0050 s. We use Eq. 4 and Eq. 5 to find the distribution of T_{rc}. With the SwitchV3.0, a 100-byte packet yields a packet time of $T = 0.01792$ s; thus, the radio turn-on time normalized to the packet time results in $\tau = 0.0084$. Fig. 11 summarizes the model parameters we empirically determine.

We setup a network of thirty SwitchV3.0 nodes, placed within a sixteen square-meter area with the gateway close to the middle, as shown in Fig. 12. The nodes are powered using batteries and emulate multiple harvester events. All nodes are programmed to generate X packets at a $g/30$ Poisson distributed arrival rate. The gateway measures the ratio of successfully received packets. The success rate at a particular load g is multiplied by g to obtain the network throughput. Based on the parameters in Fig. 11 and the Euclidean distances between the nodes in Fig. 12, we numerically compute expected state times $\underline{T^i}$, state success probabilities $P(\text{success at } i)$, and steady state probabilities π^i for a given offered load g. Then, using Eq. 1a and Eq. 1b we find the throughput and success rate at load g for the considered network topology.

We apply a similar procedure to compare the behavior of RF-DiPaQ with the expected performance of 1-CSMA, ALOHA, and np-CSMA determined using existing models [28]. Fig. 13 shows the results. The model success rate and throughput for RF-DiPaQ closely follow the measured data. At higher values of offered load g, the performance of RF-DiPaQ is limited by the average C_{RF} discharge time of the lowest charged node with pending traffic, as

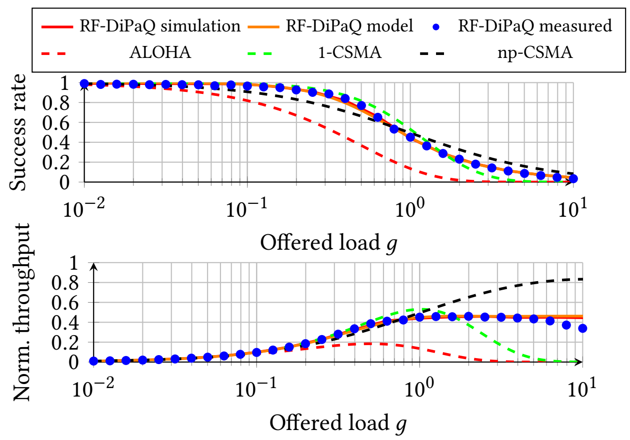

Fig. 13. Success rate (top) and normalized throughput (bottom) of the configuration in Fig. 12 comparing RF-DiPaQ model, RF-DiPaQ measurement, and baseline protocols according to their respective models [28].

this equals the non-utilized time between two consecutive transmissions. Thus, throughput of RF-DiPaQ network is expected to approach up to $1/(1 + \underline{T_{rc,1}})$ at high values of g. Fig. 13 also demonstrates that the performance of RF-DiPaQ is generally better than ALOHA and similar to 1-CSMA only up to $g = 10^0$. After that, RF-DiPaQ outperforms 1-CSMA, confirming the expectation of RF-DiPaQ superiority in higher traffic.

However, the system throughput, as shown in Fig. 13, remains constant after $g = 10^0$, whereas the performance of np-CSMA continues to improve. The plateau exists due to the relatively small number of nodes, which reduces the number of different voltages the capacitors C_{RF} are charged to. As the throughput is limited by the average discharge time between two successive transmissions and this does not depend on offered load, the throughput remains constant thereafter. On the other hand, np-CSMA would achieve this performance by spending more energy than RF-DiPaQ. We return to energy performance in Sec. 7.

6 HYBRID CIRCUIT-NETWORK SIMULATOR

While the prior graphs were obtained on the prototype devices, setting up a large-scale experimental testbed using hardware prototypes that is representative of the characteristics of the applications we target is arguably difficult. In particular, executing repeatable controlled experiments is hard, because gaining the required level of visibility into the system operation becomes a challenge when the system operation is a mixture of digital and analog functionalities. Monitoring the charge and discharge of C_{RF}, for example, without affecting the energy patterns can become increasingly impractical at large-scale.

Simulator overview. To enable an accurate, yet extensive evaluation of RF-DiPaQ, as reported in Sec. 7, we extend the open-source analog simulator Ngspice with a custom agent-based network simulator written in Python. The combination of the two allows to simulate both the analog circuitry and network capabilities of RF-DiPaQ nodes at once. Using the simulator we can quantitatively study aspects, such as the limiting conditions of throughput, and

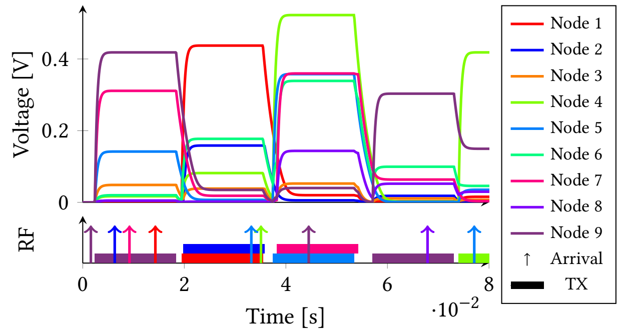

Fig. 14. The voltage levels in the reference capacitors C_{RF} of nine nodes reacting to the RF activity over time, behaving according to RF-DiPaQ.

the effects of different node placements. Using a SPICE script, the analog circuit of the RF-unit can be loaded into the simulator. When the analog circuit is not known, the relation between input power and DC output voltage may be supplied according to Eq. 2.

Simulator functioning. Fig. 14 is a snapshot of a simulation showing the RF activity of nine nodes over time, and their effect on the C_{RF}s, following the RF-DiPaQ protocol. During the simulation, the simulated wireless devices interact with each other, indicating when each device starts or stops transmitting. Based on the distance to the transmitter(s) and pathloss model, the simulator determines the voltage level that C_{RF} reaches. Based on this, transmissions are made following the RF-DiPaQ protocol. For validation, we simulate the scenario described in Sec. 5 and shown in Fig. 12, already employed to validate the model of Sec. 4. Fig. 13 also reports the simulated success rate and throughput for RF-DiPaQ. The trends obtained from the simulator closely match the model and measurement results.

7 EVALUATION

In this section, we evaluate the performance of RF-DiPaQ on a network of SwitchV3.0 nodes. We model and simulate, how state-of-the-art WuR front-end hardware would perform if used as RF-unit, show how the optimal RC value can be found, and compare the energy consumption of RF-DiPaQ to the CSMA protocols and classic Aloha. Most of our evaluation is primarily obtained from the testbed of devices, unless explicitly mentioned.

7.1 Transmission Distance

To test the effect of distance between neighboring devices on the performance of RF-DiPaQ, we placed nine Switch V3.0 RF-DiPaQ enabled nodes (Fig. 9) in a 3 by 3 grid and tested for different grid-neighbor (inter node) distances, ranging from 25 cm to 15 m. We evaluate Switch V3.0 using both voltage multiplier and log amplifier separately, as they affect the achieved sensing range.

Fig. 15 shows the success rate and the normalized throughput of different grid sizes using voltage multiplier. As expected, when using large device-to-device distances (150 cm for the Switch V3.0) the RF-units cannot sense the transmissions of other nodes, and the performance of RF-DiPaQ approaches the performance of Aloha.

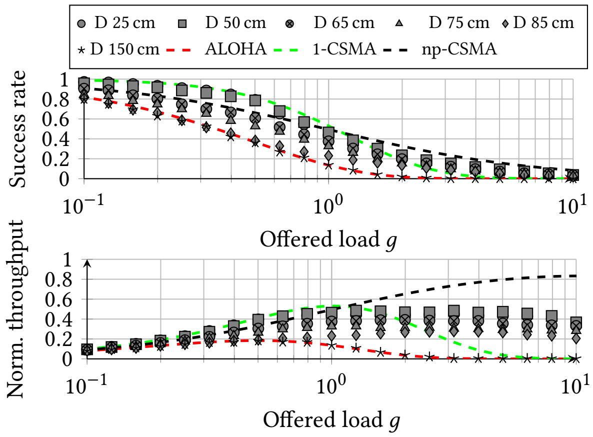

Fig. 15. Measured success rate (top) and normalised throughput (bottom) of 3 by 3 grid of 9 nodes for different node distances with voltage multiplier

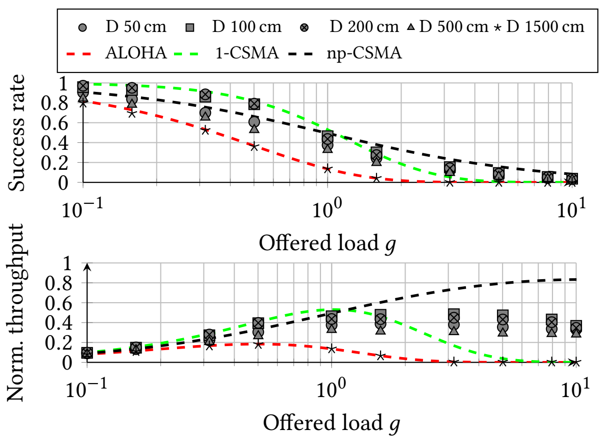

Fig. 16. Measured success rate (top) and normalised throughput (bottom) of 9 nodes for different node distances with log amplifier.

This shows the effect of the increase in the number of hidden terminals on the throughput of RF-DiPaQ. Further, as observed in Fig. 15, the shortest distance does not result in the best performance. 50 cm outperforms 25 cm, because in the 25 cm layout, the reference capacitors C_{RF} of the nodes are charged to relatively higher voltages, resulting in longer average discharge times T_{rc} between two successive transmissions, reducing the throughput.

Fig. 16 shows the success rate and normalized throughput of different grid sizes using log amplifier. In this case the nodes can sense transmissions at greater distances (up to 500 cm), and the number of hidden terminals decreases due to enhanced node sensitivity. Furthermore, the performance degrades at larger distances (from 5 m) as transmissions from nodes farther away can no longer be detected. Similar to the voltage multiplier results, at smaller distances (of less than 100 cm in this case), the network throughput is reduced due to longer discharge times T_{rc}. These results demonstrate a trade-off in terms of the energy used by the node for sensing the channel and the achieved sensitivity to other transmissions. Hence, depending on the available harvested energy and the sensing distance required for a particular use case, the choice between voltage multiplier or log amplifier can be made.

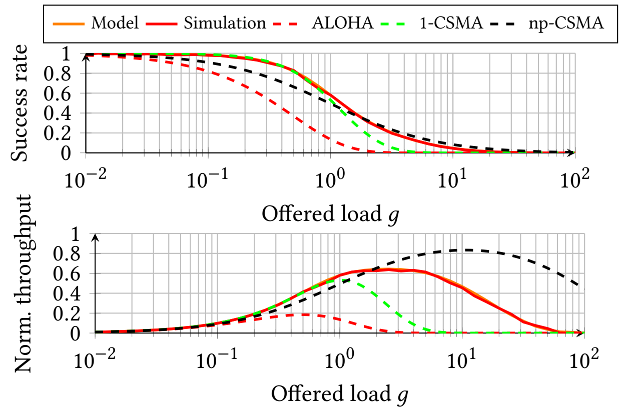

Fig. 17. Modeled success rate (top) and normalized throughput (bottom) of 100 nodes in a grid layout in a 25 m × 25 m area.

7.2 RF Unit

The performance of RF-DiPaQ depends on the RF-unit efficiency of harvesting the carrier wave and charging the capacitor. As the hardware used in WuR front-ends shares many similarities with the RF-unit, they can be re-purposed to serve as RF-unit in RF-DiPaQ scenario. Due to the unavailability of state-of-the-art WuR hardware, the model and simulation can be used to evaluate how WuR hardware would perform while serving as RF-unit. In specific, only the minimal sensitivity and the relation between DC output voltage V_{out} and input power P_{in} are needed. This allows to model the performance of the microwatt-WuR proposed by Del-Prete *et al.* [16] if adapted to serve RF-DiPaQ functionalities. The relation between V_{out} and P_{in}, is given in Eq. 19, and holds for $P_{in} \in [-70\,dBm, -35\,dBm]$. The minimal sensitivity of this hardware results in $V_{TH} = 300\,\mu V$ at an input power of -56 dBm.

$$V_{out} = 10^{aP_{in}+b}, \text{ with } a = 0.100993, b = 2.132736 \quad (19)$$

Fig. 17 shows the performance of RF-DiPaQ regarding model and simulation using 100 nodes. The nodes are positioned into a 10 by 10 node grid layout spread across a 25 m by 25 m area. Prospective use-cases involving EH-device distributions like the above can be seen inside smart factories where tens/hundreds of sensors are positioned in a few square meters and need to transmit information regarding the structural health of machinery [33] or in cases of on-demand transmissions like the ones depicted in Fig. 1 (call-crew buttons) [34]. In terms of our grid layout, the minimum distance between any pair of nodes in the network equals 2.78 m, resulting in a maximum P_{in} of less than -35 dBm, within the P_{in} range.

As shown in Fig. 17, RF-DiPaQ outperforms np-CSMA for 100 nodes and follows the 1-CSMA performance, until an offered load of $g = 0.8$. As seen in the throughput in Fig. 17, after $g = 0.8$ RF-DiPaQ outperforms 1-CSMA with a max normalized throughput of 0.64 at the saturation point $g = 2.51$, compared to 0.53 at $g = 1$ for 1-CSMA. The network under RF-DiPaQ can handle 2.46 times more offered load than 1-CSMA and 4.74 times more than Aloha in saturation. RF-DiPaQ achieves a throughput of 1.21 times more than 1-CSMA, while not consuming energy for carrier sensing, contrary to the continuous sensing in 1-CSMA. Further, RF-DiPaQ performs better than np-CSMA for lower traffic loads, i.e., till saturation.

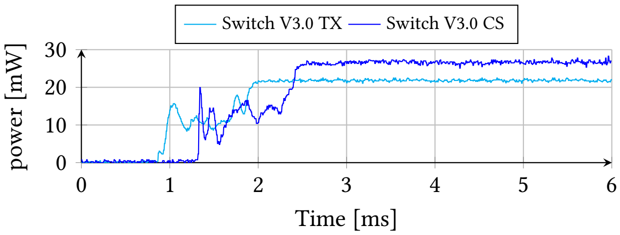

Fig. 18. Measured power consumption of the Switch V3.0, while waking up from sleep into TX and Carrier Sensing mode.

Using the same number of RF-DiPaQ nodes in smaller grids would lead to saturation at even higher values of g. As the probability of collisions depends on the standard deviation of T_{rc}, a smaller RC value could be used while maintaining the standard deviation, but reducing the mean. This would reduce the unutilized time between two successive transmissions while maintaining the probability of collisions, thus increasing the saturation point.

This model and simulation are based on the hardware of -56 dBm WuR [16], as from this hardware the relation between V_{out} and P_{in} became known. Although there are more sensitive WuR designs, like the -79.1 dBm WuR proposed by Mangal *et al.* [35], their relation between V_{out} and P_{in} is not known and, therefore, cannot be modeled or simulated in networks of RF-DiPaQ nodes. Nevertheless, RF-DiPaQ nodes with a -79.1 dBm RF-unit would result in a significantly larger range. The RF-DiPaQ MAC protocol does not need semantic-addressing; just the carrier wave detection. Thus, no sensitivity has to be used to decode the wake up call. Therefore, the hardware of the state-of-the-art WuRs [17, 24, 35, 36] achieves even higher sensitivity when used as RF-units in RF-DiPaQ scenarios.

7.3 Energy Consumption

RF-DiPaQ also outperforms 1-CSMA regarding energy usage. Regarding throughput in Fig. 17, when RF-DiPaQ saturates at an offered load of $g = 2.51$, nodes following 1-CSMA spend on average 60% of the packet time T sensing the medium, waiting to transmit. This results in 2.17 times higher energy usage than in RF-DiPaQ, even when not accounting for success rate. Fig. 18 shows the power trace of the Switch V3.0 (Fig. 9) while waking up to transmit/sense the channel, showing the power consumption for transmitting and carrier sensing to be 22 mW and 27 mW, respectively. For this hardware, at this load, the average energy usage per arrival equals 815.10 μJ in 1-CSMA and 374.00 μJ in RF-DiPaQ. Apart from the above mentioned amount of saved energy which is due to zero energy sensing, RF-DiPaQ also evades collisions by prioritizing transmissions based on distance. These collisions would lead 1-CSMA to consume more energy to retransmit (See Fig. 19).

Regarding np-CSMA, energy consumption due to sensing depends on the frequency and duration of sensing (i.e., back-off intervals). Assuming a CCA of 0.15 ms, the Switch V3.0 consumes a minimum of 20.66 μJ per assessment. The probability of a packet arriving at a busy medium equals $p = 1/(1+1/g)$. Using the expected value of the geometric distribution, the expected number of failed assessments before transmitting can be calculated to $1/(1-p)-1$. For the Switch V3.0 hardware at an offered load of $g = 2.51$ this results in 2.51 tries before transmitting, resulting in an average of 486.72 μJ consumed per packet. This amount still exceeds the consumed energy per packet of RF-DiPaQ, also taking the success rate into account results the data as seen in Fig. 19. As traffic load g increases RF-DiPaQ outperforms the 1-CSMA protocol by a higher factor regarding energy consumption. For example, at $g = 1$, wherein the throughput of the 100 nodes simulated in Sec. 7.2 is above 0.6, 1-CSMA and np-CSMA consume 819.31 μJ and 848.82 μJ, respectively, while the consumption of RF-DiPaQ equals 645.05 μJ, as shown in Fig. 19. When specifically compared to np-CSMA, RF-DiPaQ consumes 36% less energy at an offered load of $g = 0.5$, while 10% less at $g = 2$.

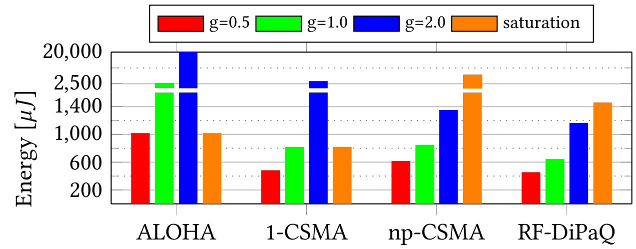

Fig. 19. Energy per successful packet transmission for different MAC protocols for different offered load values.

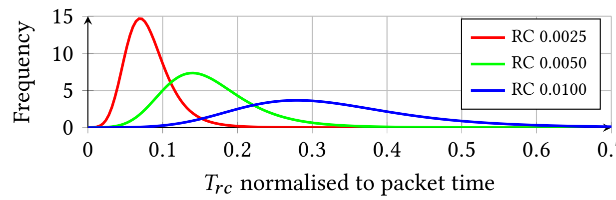

Fig. 20. T_{rc} distribution of a large network for different RC values.

7.4 Selection of R_{RF} and C_{RF}

To optimize RF-DiPaQ performance the optimal RC value needs to be found. Besides the threshold level and the voltage to which the reference capacitors C_{RF} are charged, the RC value affects the discharge time. A relatively larger RC value results in longer average discharge times. As the discharge time between two successive transmissions cannot be utilized, this limits the network throughput. Apart from the average discharge time, the RC value also influences its variance. Lower RC values result in a smaller discharge time variance, increasing the probability of two pending nodes having the same discharge time, causing a collision.

Fig. 20 shows the effect of the RC value on the T_{rc} discharge distribution calculated with Eq. 5. A larger RC value both increases the mean and deviation of T_{rc}. However, a lower average discharge time also lowers the probability of an arriving packet finding a busy medium. At low values of offered load g, this increases the success rate, making RF-DiPaQ match 1-CSMA for RC values up to 1ms, as shown in Fig. 21. The optimal RC value is small enough to not result in overly large average discharge times, and large enough to not result in many collisions. Fig. 21 shows the success rate and throughput of the Switch V3.0 in the scenario described in Sec. 5 for different RC values. As seen in the throughput in Fig. 21, the RC value of 0.0050 s results in optimal performance. When the RC value is increased (0.0100 s and 0.0200 s) the maximum throughput is reduced. When the RC value is decreased (0.0010 s and 0.0005 s)

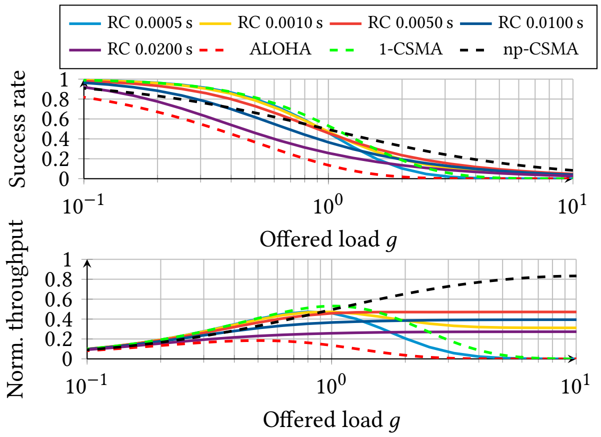

Fig. 21. Success rate (top) and normalized throughput (bottom) of nine nodes in a grid layout of 1 m×1 m for different RC values.

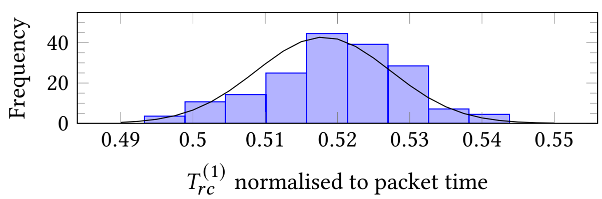

Fig. 22. Effect of noise on measured discharge time, $T_{rc}^{(1)}$, of a single node receiving from a single transmitter; Gaussian fit with the standard deviation of 0.009.

the probability of collisions increases, reducing the throughput at higher levels of offered load g.

7.5 Influence of Noise

The selected TS881 comparator has an input hysteresis of 2.4 mV, which prevents its output from oscillating between rails due to noise, when the input voltage matches the reference voltage. Noise however affects the minimum charge levels across C_{RF}, as the in-band noise floor charges the capacitors. If V is always above V_{TH} then the node assumes the medium is busy and never transmits, if it is below V_{TH} the node is unaffected. As V_{TH} can be tuned, it can be set properly in noisy environments to circumvent the issue.

Noise also has an effect on the charge level while receiving a transmission, affecting the discharge time. To evaluate this, two nodes were placed at 10 cm distance, one programmed to transmit and the other to measure and report its discharge times, $T_{rc}^{(1)}$, which is the T_{rc} of a single transmitter-receiver pair. $f_{T_{rc}^{(1)}}$ and $F_{T_{rc}^{(1)}}$ are the PDF and CDF of the Gaussian fit. The probability of collision at equal distance from the previous transmitter is,

$$P_{ceq} = \int_0^{\infty} f_{T_{rc}^{(1)}}(x) \cdot (F_{T_{rc}^{(1)}}(x+0.008) - F_{T_{rc}^{(1)}}(x-0.008))dx. \quad (20)$$

Fig. 22 shows the measured discharge times and the effect of noise on the deviation. By fitting a Gaussian distribution, we found Standard deviation to be 0.009. With $\tau = 0.0084$ (see Sec. 4.3), which is the time two nodes must differ in discharge times to avoid a collision, P_{ceq} is 0.455. However, the probability of two nodes being exactly equidistant from a transmitter is very low and decreases exponentially with the number of nodes (assuming a constant network load), e.g., with 10 nodes it is 0.0003.

7.6 Effects of Multipath

As expected, RF-DiPaQ performs well in clear environments but even in multipath scenarios its performance does not deteriorate. The randomness inserted in the charging level across C_{RF} of the nodes increases the deviation of T_{rc} without increasing the mean (Sec. 7.4), resulting in better performance.

(a) Multipath effect in Fuselage **(b)** Open field

Fig. 23. Setup in different terrains.

Fig. 24 shows the measured success rate and normalized throughput of the same network in the fuselage of an aircraft and in an open field. Due to low sensitivity of the voltage multiplier, the contribution of multipath is small. As RF waves bounces of nearby object often doubles the distance between transmitter/receiver exceeding the minimum sensitivity resulting in limited differences.

8 DISCUSSION

Fairness. As the charge in the capacitors of the RF-DiPaQ nodes determines the order in which nodes are allowed to transmit (lowest charged node first), nodes that are charged higher more often have a reduced chance to transmit compared to nodes that are charged lower more often. For a network laid out in a grid, this results in nodes in the middle of the network having reduced performance since these nodes have more close-by neighbors compared to the nodes at the edge of the network. However, this apparent unfairness does not affect if the harvested energy is sufficient to keep the device on till it gets the chance to transmit.

This unfairness due to position can however be corrected by adapting T_{rc} – the RC discharge parameter. By increasing the RC values for the nodes near the edge of the network, their discharge time is increased to equal the discharge time of the nodes in the middle of the network that are charged to a higher value.

We performed multiple experiments on our simulation platform to find insight regarding the unfairness. The effect of this correction is shown Fig. 25, Where the top-two sub-figures show the lack of fairness without the RC correction, and the bottom-two the fairness with the RC correction. As expected without the RC correction, nodes in the middle of the network are disadvantaged and perform poorly. While with the RC correction the performance of a node does not depend on its location.

Low-power MACs and communication patterns. Our technique works well with small energy budgets, generated by event-based energy harvesting solutions like a switch. The nature of event-based harvesting in this one-shot context implies that only simple CSMA and ALOHA are practical in such systems. More complex

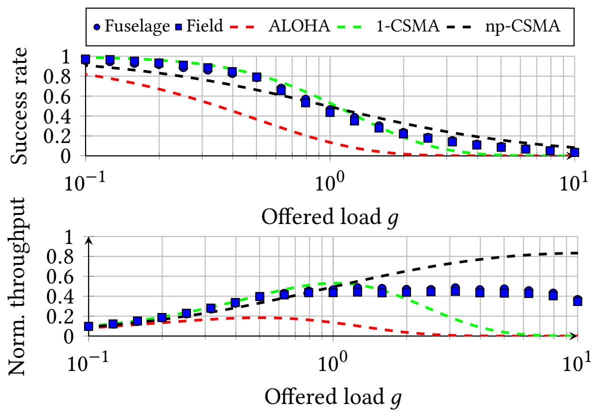

Fig. 24. Measured success rate (top) and normalised throughput (bottom) of a network of 9 nodes inside a fuselage and outside in an open field Fig. 23, showing the effect of multipath.

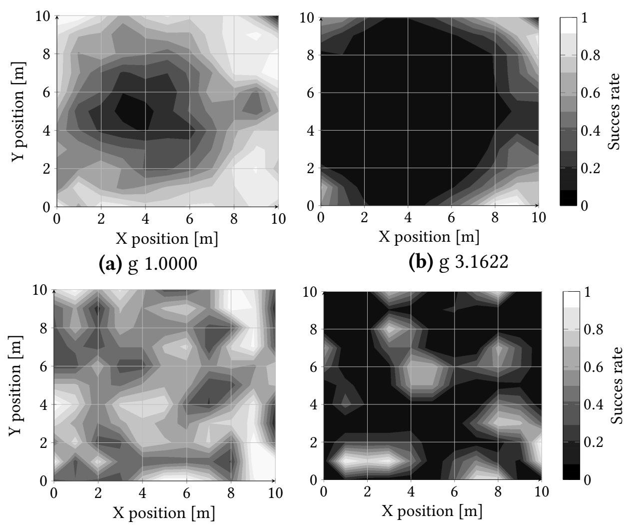

(a) g 1.0000 **(b)** g 3.1622 **(c)** g 1.0000 **(d)** g 3.1622

Fig. 25. Positional fairness for load g = 1.000 (a and c) and g = 3.1622 (b and d), for a network without (a and b) and with (c and d) RC correction.

MAC protocols require more resources, especially in terms of energy, to implement functionality like mult-message handshaking. These protocols usually use a back-off mechanism which requires more energy and repeated carrier sensing, neither of which is feasible in this context. Thus, we considered CSMA and ALOHA for benchmarking.

Our work also considers only the communication from the sensor devices to a one-hop gateway. This follows directly from the fact that the system cannot back-off repeatedly or continuously listen since the harvested energy is too low. This highly limits the scope of many-to-many or downlink schemes. However, we envision a protocol where, after a node transmits, it can briefly listen (depending on the harvested energy) for a reply from the gateway. This allows for example an application where an energy harvesting switch equipped with an e-ink display uses the response received from the gateway. Further, having multiple gateways is a simple extension that can increase success rate.

Limitations. RF-DiPaQ can be extended to a large scale deployment albeit only when the offered load is low as any re-transmission already exceeds the small energy budget. The limiting factor for scalability then becomes not the number of nodes in a network but the offered network load g.

Further, even though modern MCU's consume power in the order of 100 nano-watts, there is still a limited budget of energy available to the node. Thus there is a limited amount of time a node can stay in a deep sleep setting before it must transmit anyways.

9 CONCLUSION

RF information harvesting allows wireless embedded sensing devices to detect channel activity at essentially no energy cost. This feature becomes an asset in an emerging class of event-driven wireless sensing applications, composed of energy-harvesting devices operating with tiny energy budgets.

The RF-DiPaQ protocol integrates RF information harvesting. We detailed and analytically modeled the design of RF-DiPaQ, created a real-world hardware/software prototype and developed a hybrid circuit-network simulator to evaluate the protocol performance in conditions as close to reality as possible, yet without the practical limitations due to setting up repeatable controlled experiments. Our results indicate that RF-DiPaQ outperforms 1-CSMA with a maximum normalized throughput of 0.64 at the saturation point $g = 2.51$, compared to 0.53 at $g = 1$ for 1-CSMA. The network under RF-DiPaQ can handle 2.46 times more offered load than 1-CSMA and 4.74 times more than Aloha in saturation. Furthermore, when compared to np-CSMA, which is best performing among p-CSMA, np-CSMA and 1-CSMA, RF-DiPaQ consumes 36% less energy at offered load $g = 0.5$, while 10% less at $g = 2$.

Acknowledgments. This work was funded by the InSecTT (www.insectt.eu) project that has received funding from the ECSEL Joint Undertaking (JU) under grant agreement #876038 and by the Swedish Foundation for Strategic Research (SSF). JU receives support from the European Union's Horizon 2020 research and innovation programme and Austria, Sweden, Spain, Italy, France, Portugal, Ireland, Finland, Slovenia, Poland, Netherlands, Turkey. The document reflects only the author's view and the Commission is not responsible for any use that may be made of the information it contains.

REFERENCES

[1] S. Sudevalayam and P. Kulkarni, "Energy harvesting sensor nodes: Survey and implications," *IEEE Comm. Surveys and Tutorials*, vol. 13, no. 3, pp. 443–461, 2011.
[2] S. Gună, L. Mottola, and G. P. Picco, "Dice: Monitoring global invariants with wireless sensor networks," *ACM Trans. on Sensor Networks*, vol. 10, no. 4, 2014.
[3] J. C. Kwan and A. O. Fapojuwo, "Radio Frequency Energy Harvesting and Data Rate Optimization in Wireless Information and Power Transfer Sensor Networks," *IEEE Sensors Journal*, vol. 17, no. 15, pp. 4862–4874, 2017.
[4] J. C. Rodriguez, V. Nico, and J. Punch, "Powering wireless sensor nodes for industrial iot applications using vibration energy harvesting," in *2019 IEEE 5th World Forum on Internet of Things (WF-IoT)*, 2019, pp. 392–397.
[5] A. Kansal, J. Hsu, S. Zahedi, and M. B. Srivastava, "Power management in energy harvesting sensor networks," *ACM Transactions on Embedded Computing Systems (TECS)*, vol. 6, no. 4, pp. 32–es, 2007.
[6] S. Ulukus, A. Yener, E. Erkip, O. Simeone, M. Zorzi, P. Grover, and K. Huang, "Energy harvesting wireless communications: A review of recent advances," *IEEE JSAC*, vol. 33, no. 3, pp. 360–381, 2015.
[7] H. H. R. S. et al., "A comprehensive review on energy harvesting MAC protocols in WSNs: Challenges and tradeoffs," *Ad Hoc Networks*, vol. 71, 2018.
[8] M. L. Wymore and D. Qiao, "RIVER-MAC: A Receiver-Initiated Asynchronously Duty-Cycled MAC Protocol for the Internet of Things," in *2019 IEEE 43rd Annual Computer Software and Applications Conference*, vol. 1, 2019, pp. 860–869.

[9] X. L. et al., "Wireless Networks With RF Energy Harvesting: A Contemporary Survey," *IEEE Comm. Sur. and Tut.*, vol. 17, no. 2, pp. 757–789, 2015.
[10] J. Ren, J. Hu, D. Zhang, H. Guo, Y. Zhang, and X. Shen, "RF Energy Harvesting and Transfer in Cognitive Radio Sensor Networks: Opportunities and Challenges," *IEEE Communications Magazine*, vol. 56, no. 1, pp. 104–110, 2018.
[11] M. Y. Naderi, P. Nintanavongsa, and K. R. Chowdhury, "RF-MAC: A Medium Access Control Protocol for Re-Chargeable Sensor Networks Powered by Wireless Energy Harvesting," *IEEE Trans. on Wireless Comm.*, vol. 13, no. 7, 2014.
[12] D. T. Hoang, D. Niyato, P. Wang, and D. I. Kim, "Opportunistic Channel Access & RF Energy Harvesting in Cognitive Radio Networks," *IEEE JSAC*, vol. 32 - 11, 2014.
[13] Y. H. Bae and J. W. Baek, "Sensing Strategy Exploiting Channel Memory in CR Network With RF Energy Harvesting," *IEEE Communications Letters*, vol. 22, no. 12, pp. 2539–2542, 2018.
[14] T. Ha, J. Kim, and J. Chung, "HE-MAC: Harvest-Then-Transmit Based Modified EDCF MAC Protocol for Wireless Powered Sensor Networks," *IEEE Transactions on Wireless Communications*, vol. 17, no. 1, pp. 3–16, 2018.
[15] M. M. . V. J. . B. S. . V. B. . E. P. . L. Benini, "Design, Implementation, & Performance Evaluation of a Flexible Low-Latency Nanowatt Wake-Up Radio Receiver," *IEEE Transactions on Industrial Informatics*, vol. 12 - 2, 2016.
[16] M. Del Prete, A. Costanzo, M. Magno, D. Masotti, and L. Benini, "Optimum Excitations for a Dual-Band Microwatt Wake-Up Radio," *IEEE Transactions on Microwave Theory and Techniques*, vol. 64, no. 12, pp. 4731–4739, 2016.
[17] D. Spenza, M. Magno, S. Basagni, L. Benini, M. Paoli, and C. Petrioli, "Beyond duty cycling: Wake-up radio with selective awakenings for long-lived wireless sensing systems," in *IEEE ICC*, 2015, pp. 522–530.
[18] T. N. Le, M. Magno, A. Pegatoquet, O. Berder, O. Sentieys, and E. Popovici, "Ultra Low Power Asynchronous MAC Protocol Using Wake-up Radio for Energy Neutral WSN," in *Proceedings of the 1st International Workshop on Energy Neutral Sensing Systems*. Association for Computing Machinery, 2013.
[19] J. Oller, I. Demirkol, J. Casademont, J. Paradells, G. U. Gamm, and L. Reindl, "Wake-up Radio as an Energy-Efficient Alternative to Conventional Wireless Sensor Networks MAC Protocols," in *Proc.of 16th ACM International Conference on Modeling, Analysis & Simulation of Wireless and Mobile Systems*. ACM, 2013.
[20] M. Zgaren and M. Sawan, "A high-sensitivity battery-less wake-up receiver for 915 MHz ISM band applications," in *IEEE ICECS*, 2015, pp. 336–339.
[21] J. M. et al., "A -106dBm 33nW Bit-Level Duty-Cycled Tuned RF Wake-up Receiver," in *2019 Symposium on VLSI Circuits*, 2019, pp. C86–C87.
[22] C. S. et al., "Optimizing sensor networks in the energy-latency-density design space," *IEEE Trans. on Mob. Comp.*, vol. 1, no. 1, pp. 70–80, 2002.
[23] H. Karvonen, J. Petäjäjärvi, J. Iinatti, M. Hämäläinen, and C. Pomalaza-Ráez, "A generic wake-up radio based MAC protocol for energy efficient short range communication," in *2014 IEEE 25th Annual International Symposium on Personal, Indoor, and Mobile Radio Communication (PIMRC)*, 2014, pp. 2173–2177.
[24] D. Ghose, F. Y. Li, and V. Pla, "MAC Protocols for Wake-Up Radio: Principles, Modeling and Performance Analysis," *IEEE Transactions on Industrial Informatics*, vol. 14, no. 5, pp. 2294–2306, 2018.
[25] B. Lucia, V. Balaji, A. Colin, K. Maeng, and E. Ruppel, "Intermittent computing: Challenges and opportunities," in *2nd Summit on Advances in Programming Languages*. Schloss Dagstuhl-Leibniz-Zentrum fuer Informatik, 2017.
[26] S. Ahmed, N. A. Bhatti, M. H. Alizai, J. H. Siddiqui, and L. Mottola, "Efficient intermittent computing with differential checkpointing," in *Proceedings of the 20th ACM SIGPLAN/SIGBED International Conference on Languages, Compilers, and Tools for Embedded Systems*, 2019.
[27] V. Liu, A. Parks, V. Talla, S. Gollakota, D. Wetherall, and J. R. Smith, "Ambient backscatter: Wireless communication out of thin air," *ACM SIGCOMM Computer Communication Review*, vol. 43, no. 4, pp. 39–50, 2013.
[28] S. Y. Cheung, "Performance Analysis of the unslotted 1-persistent CSMA protocol," mathcs.emory.edu/~cheung/Courses/558/Syllabus/00/CSMA/csma-anal1a.
[29] G. Casella and R. Berger, *Statistical Inference*, ser. Duxbury advanced series in statistics and decision sciences. Thomson Learning, 2002.
[30] ZF Switch, "TIDA-00690," https://www.ti.com/tool/TIDA-00690.
[31] P. N. et al., "Design Optimization and Implementation for RF Energy Harvesting Circuits," *IEEE Jour. on Emerg. & Sel. Topics in Circuits & Systems*, vol. 2-1, 2012.
[32] Texas Instruments, "CC1352R product page," ti.com/product/CC1352R#.
[33] ericsson.com, "Realizing smart manufacturing through IoT," ericsson.com/en/mobility-report/articles/realizing-smart-manufact-iot, [accessed: 2020-06-07].
[34] N. K. et al., "Pushing the Boundaries of IoT: Building and Testing Self-powered Batteryless Switch," in *IEEE WF-IoT*, 2019, pp. 231–236.
[35] V. Mangal and P. R. Kinget, "28.1 A 0.42nW 434MHz -79.1dBm Wake-Up Receiver with a Time-Domain Integrator," in *IEEE ISSCC*, 2019, pp. 438–440.
[36] R. Piyare, A. L. Murphy, C. Kiraly, P. Tosato, and D. Brunelli, "Ultra Low Power Wake-Up Radios: A Hardware and Networking Survey," *IEEE Comm. Sur. and Tut.*, vol. 19, no. 4, pp. 2117–2157, 2017.